Green Chemistry

PAPER

View Article Online
View Journal | View Issue

Cite this: *Green Chem.*, 2025, **27**, 13323

Porous core–shell CuAu@Cu_2O catalyst for acidic C–N coupling toward urea electrosynthesis from CO_2 and nitrate

Xiang Ji, Yaodong Yu, Yujia Guan, Jianping Lai * and Lei Wang *

Received 8th August 2025,
Accepted 22nd September 2025

DOI: 10.1039/d5gc04150c

rsc.li/greenchem

Traditional neutral/alkaline systems face limitations due to incompatibility with acidic industrial wastewater and spontaneous carbonate byproduct formation, causing reactant depletion and low efficiency. While acidic conditions enhance industrial applicability, challenges persist: insufficient adsorption energy for key intermediates, hydrogen evolution reaction (HER) competition, and catalyst corrosion. This study developed a porous core–shell CuAu@Cu_2O catalyst, achieving 55.4% faradaic efficiency and 1824.8 μg h^{-1} mg^{-1} urea yield at −0.5 V *vs.* RHE in acidic media, with 100-hour stability. Mechanistic insights reveal that Cu/Au dual sites synergistically activate CO_2 and NO_3^-, lowering *COOH/*NOH intermediate adsorption energies; the Cu_2O shell regulates proton supply *via* Au-mediated electronic effects, promoting C–N coupling while suppressing the HER; and charge redistribution from Cu to Au at the porous interface stabilizes the catalyst structure. This work not only provides an efficient catalyst for urea electrosynthesis under acidic conditions, but also pioneers a novel 'waste-treating-waste' green synthesis paradigm, offering new insights for electrochemical manufacturing in the context of carbon neutrality goals.

Green foundation

1. We pioneer acid-tolerant electrocatalytic urea synthesis by coupling CO_2 valorization with acidic nitrate wastewater treatment. This approach overcomes the limitations of carbonate precipitation, reactant loss and wastewater incompatibility and bypasses the Haber–Bosch process.
2. CuAu@Cu_2O enables the direct conversion of acidic nitrate wastewater and CO_2 into urea without the need for pH adjustment, while maintaining operational stability for 100 hours under mild potentials.
3. For more sustainable development, future efforts could focus on replacing the oxygen evolution reaction with value-added anodic oxidations and scaling up the process using flow cells or membrane assembly devices to further reduce energy consumption.

Introduction

The widespread utilization of urea in agriculture and industrial sectors contrasts sharply with its energy-intensive production through conventional Haber–Bosch and Bosch–Meiser routes, which involve multi-step ammonia synthesis and subsequent urea conversion under extreme conditions, resulting in massive energy consumption and CO_2 emissions.[1–5] Electrochemical C–N coupling of CO_2 and nitrate has emerged as a promising green alternative for direct urea synthesis, yet existing systems predominantly operate in neutral/alkaline media.[6–9] These environments suffer from irreversible CO_2 loss through carbonate precipitation and incompatibility with nitrate sources in acidic industrial wastewater.[10–13] While acidic conditions inherently mitigate carbonate formation, they introduce critical challenges including sluggish intermediate reactivity, overwhelming hydrogen evolution competition, and structural degradation of catalysts.[1,14–18]

The complexity of electrocatalytic urea synthesis arises from its multi-step mechanism involving CO_2 reduction to *CO (*via* *COOH intermediates), nitrate reduction to *NH_2 (*via* *NOH pathways), and subsequent C–N coupling – all requiring precise regulation of 16-electron transfer processes.[19–22] Recent advances highlight multi-active-site engineering as an effective strategy to optimize distinct reaction steps.[1,23,24] Core–shell structures like Au@Cu_2O can create a charge

State Key Laboratory Base of Eco-Chemical Engineering, Ministry of Education, International Science and Technology Cooperation Base of Eco-Chemical Engineering and Green Manufacturing, College of Chemistry and Molecular Engineering, Qingdao University of Science and Technology, Qingdao 266042, P. R. China.
E-mail: jplai@qust.edu.cn, inorchemwl@126.com

barrier to mitigate acidic corrosion.[11] Considering the above-mentioned points, the design of core–shell catalysts with multiple active sites is anticipated to resolve the intertwined challenges of activity, selectivity, and stability in acidic C–N coupling systems. Here, we designed a porous CuAu@Cu_2O core–shell catalyst that achieves 55.4% faradaic efficiency and 1824.8 μg h^{-1} mg^{-1} urea yield in weakly acidic media (pH = 3, −0.5 V *vs.* RHE). Au and Cu components respectively reduce the adsorption energies of *COOH and *NOH intermediates, thereby generating *CO and *NH_2, while Cu_2O phases modulate the hydrogen adsorption strength to balance proton supply and HER suppression. Charge redistribution from Cu to Au at their interface, driven by electron transfer, achieves dual catalytic enhancements: it stabilizes Cu^+ species to suppress disproportionation while simultaneously optimizing interfacial activity through d-band center modulation of Au. Specifically, the downward-shifted d-band center strengthens CO_2 adsorption/activation, whereas precisely tuned hydrogen adsorption energy barriers steer the reaction pathway toward favorable CO_2 hydrogenation over the competing hydrogen evolution reaction (HER). This synergistic mechanism achieves dual modulation of catalytic selectivity at the electronic structure level. This breakthrough establishes the first efficient acidic electrocatalytic system for direct CO_2–nitrate coupling while demonstrating a material design paradigm that integrates intermediate optimization, HER suppression, and structural stabilization. The work provides fundamental principles for multi-active-site catalyst engineering and practical strategies for valorizing acidic wastewater in sustainable urea synthesis.

Results and discussion

Synthesis and structural characterization of CuAu, Cu@Cu_2O, Au@Cu_2O and CuAu@Cu_2O

In a typical synthesis, a CuAu alloy was prepared *via* $NaBH_4$-mediated co-reduction of $CuCl_2$ and $HAuCl_4$, followed by annealing under a reducing atmosphere to obtain the bimetallic catalyst, with its composition confirmed by ICP-OES (Table S1). Subsequent Ar/O_2 annealing partially oxidized the surface to form Cu_2O, as evidenced by SEM/TEM images revealing spherical nanoparticles with porous shells (Fig. 1a, b and S1). During oxide formation, surface Cu reduction induced lattice distortion through volume shrinkage/expansion. The micropore structure facilitates reactant diffusion to the core surface while providing additional adsorption sites along the inner walls of the shell channels. Lattice fringe analysis highlighted an outer layer spacing of 0.268 nm (Cu_2O), contrasting with the inner 0.212 nm spacing of the CuAu alloy core (Fig. 1c–e). EDS mapping confirmed the core–shell architecture and uniform Cu/Au distribution in the oxide shell (Fig. 1f).[25–27] Comparative synthesis of CuAu, Cu@Cu_2O, and Au@Cu_2O (Fig. S2–S4) showed analogous structural characteristics, validating the reproducibility of both facet structures and core–shell configurations.

The XRD patterns of CuAu@Cu_2O (Fig. 2a and S5) exhibit dominant diffraction features corresponding to Cu(111) and Cu_2O(111). Notably, the Cu(111) peak displays a negative shift compared to that of Cu@Cu_2O, indicating an expanded *d*-spacing. This lattice expansion arises from the incorporation of Au atoms into the Cu lattice to form a CuAu alloy, as sup-

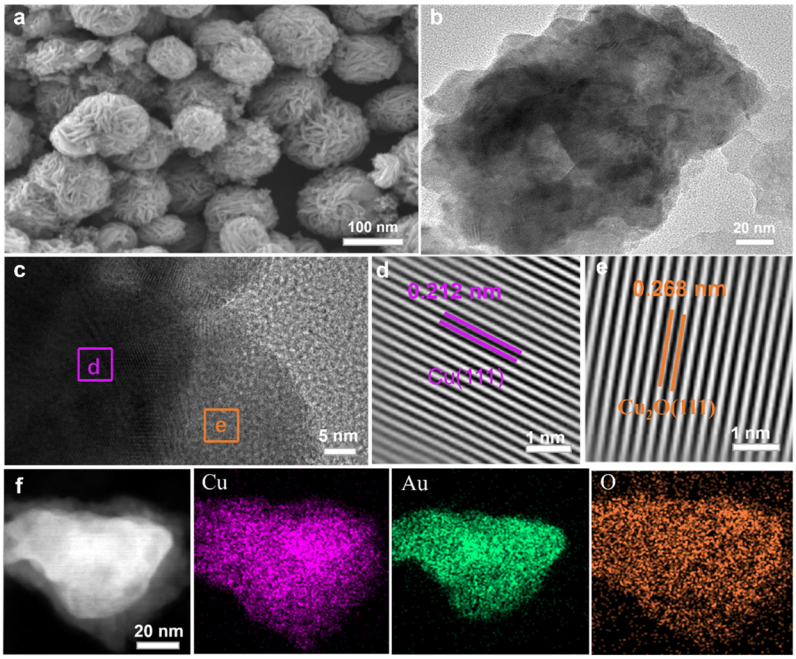

Fig. 1 Morphology of CuAu@Cu_2O. (a) SEM image. (b) TEM image of CuAu@Cu_2O. (c) HRTEM image of CuAu@Cu_2O. (d, e) IFFT patterns of the selected CuAu@Cu_2O. (f) TEM-EDX elemental mapping images of CuAu@Cu_2O.

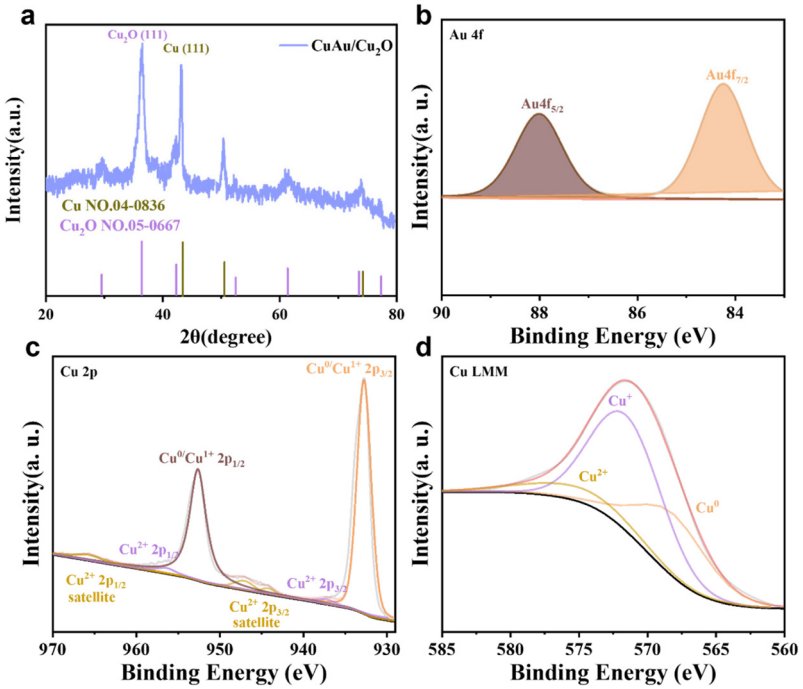

Fig. 2 Structure of CuAu@Cu_2O. (a) XRD of CuAu/Cu_2O. (b) Au 4f, (c) Cu 2p, and (d) Cu LMM XPS spectra of CuAu/Cu_2O.

ported by HRTEM analysis.[28] The persistent Cu_2O(111) peak confirms the retention of a Cu_2O phase in the outer shell, collectively demonstrating the successful construction of a core–shell architecture. XPS analysis further clarifies the electronic states of the constituent elements. The Au $4f_{7/2}$ peak at 84.2 eV corresponds to metallic Au(0) (Fig. 2b), confirming the non-oxidized state of Au within the alloyed core. The Cu $2p_{3/2}$ peak at 932.7 eV aligns closely with the characteristic binding energy of Cu^+ in Cu_2O (933.0 eV) (Fig. 2c), suggesting the coexistence of Cu^+ and Cu(0) species in the shell.[29,30] This conclusion is further reinforced by the Cu Auger LMM peak at 572.3 eV (Fig. 2d), providing complementary evidence for the stable presence of both +1 and 0 oxidation states of copper.[10,31]

The electronic structure of CuAu@Cu_2O was investigated using UPS and UV-Vis diffuse reflectance spectroscopy. These analyses reveal that the synergistic modulation of the direct bandgap (~2.68 eV) and valence band maximum (VBM, ~1.83 eV) (Fig. S6) in CuAu@Cu_2O enables precise alignment of its conduction band minimum (CBM, ~−0.85 eV) (Fig. S7) with the thermodynamic potential window (−0.4 V *vs.* RHE) required for NO_3^- reduction (to NH_2) and CO_2 activation.[32–34] The superior reduction potential of nitrate suppresses the HER, directing adsorbed *H species to preferentially participate in C–N coupling.[34] Concurrently, the electronic interaction between Au and Cu_2O induces a significant reduction in work function ($\Delta\Phi$ = 0.42 eV, Fig. S8), shifting the Fermi level toward the valence band.[35] This interfacial charge redistribution generates a surface dipole, which, combined with the plasmonic coupling effect of Au, further weakens the H^+ adsorption energy barrier ($\Delta G\_H \rightarrow 0$), steering *H toward urea synthesis rather than the HER.[36]

The core–shell architecture drives interfacial electron transfer through the work function difference between Au and Cu, resulting in electron enrichment at Au and depletion at Cu^+. This not only suppresses the Cu^+ disproportionation reaction ($2Cu^+ \rightarrow Cu^{2+} + Cu^0$), but also optimizes intermediate adsorption energies through the CuAu alloy core, synergizing with the selective inhibition effect of the Cu_2O shell to endow the material with high catalytic activity and stability. Such electronic structure optimization enhances the charge transfer efficiency while suppressing competitive side reactions (HER) and reducing kinetic barriers in key steps, significantly improving both selectivity and catalytic activity for urea synthesis. This establishes an efficient electron-energy cooperative regulation mechanism for multi-proton-coupled C–N coupling reactions.

Electrochemical performance

The co-electrolysis of CO_2 and nitrate was performed in a gas-tight H-type electrolytic cell using chronoamperometry (CA) at pH = 3 adjusted with sulfuric acid. As shown in Fig. S9, linear sweep voltammetry (LSV) curves in a CO_2-saturated aqueous electrolyte containing potassium nitrate exhibit enhanced current density, indicating electrocatalytic C–N coupling and confirming active CO_2–NO_3^- interactions. Controlled potential electrolysis (−0.3 to −0.7 V *vs.* RHE) was conducted, with products analyzed by gas chromatography (gaseous products), UV-Vis spectroscopy (liquid products, Fig. S10–S12), and ^1H NMR (Fig. S13). UV-Vis spectra (Fig. S14 and S15) reveal that

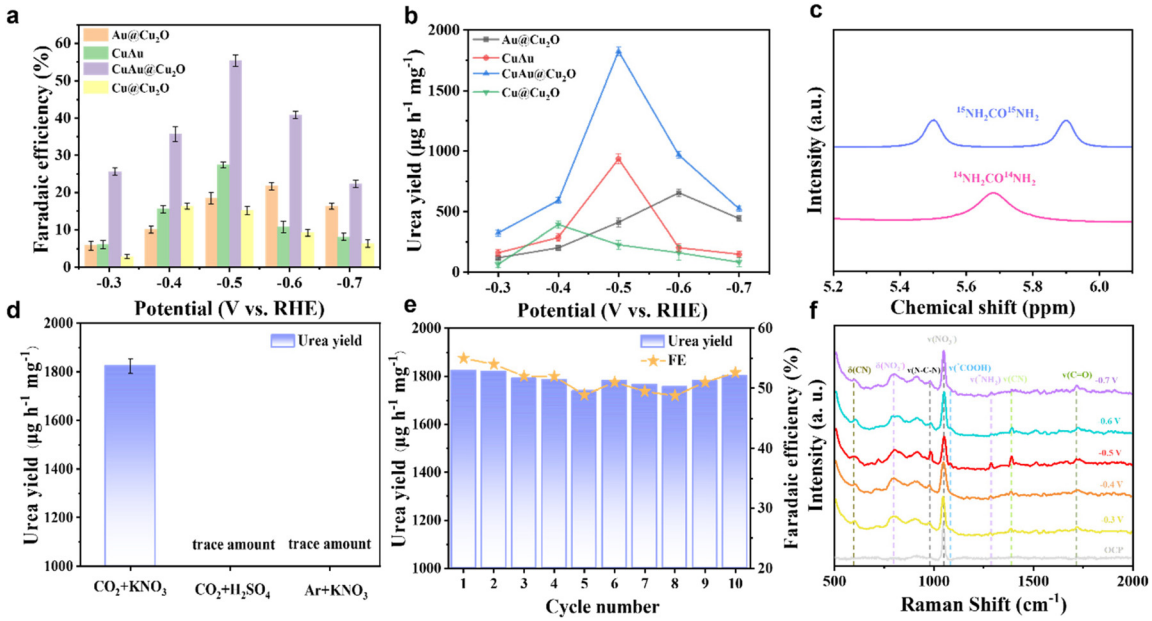

Fig. 3 Electrocatalytic performances and *Operando* spectroscopy measurement for urea synthesis. (a) Urea FE and (b) urea production rate of CuAu@Cu_2O, CuAu, Cu@Cu_2O, and Au@Cu_2O at various applied potentials. (c) ^1H NMR spectra of the electrolyte obtained in isotope labeling experiments. (d) Control experiment results of CuAu@Cu_2O at −0.5 V *versus* RHE. (e) Stability test results of the reaction of CuAu@Cu_2O. (f) *In situ* surface-enhanced Raman spectra recorded at different potentials for CuAu@Cu_2O, CuAu, Cu@Cu_2O, and Au@Cu_2O during urea electrochemical synthesis.

the optimal potential is −0.5 V, with CuAu@Cu_2O achieving the highest urea yield. Notably, CuAu@Cu_2O exhibits superior current density across the applied potential range compared to Cu@Cu_2O and CuAu counterparts (Fig. S16), demonstrating its exceptional electrocatalytic activity for urea synthesis.[37]

Competing side reactions (*e.g.*, NO_3^-RR, CO_2RR, and HER) suppress the co-reduction of CO_2 and NO_3^- to urea, resulting in a complex product distribution (Fig. S17), including urea, ammonia, nitrite, H_2, and CO, with a near 100% total faradaic efficiency. The urea faradaic efficiency follows a volcano-shaped dependence on the applied potential (Fig. 3a and b), peaking at 55.4% for CuAu@Cu_2O at −0.5 V *vs.* RHE, corresponding to a production rate of 1824.8 μg h^{-1} mg^{-1}, outperforming most reported electrocatalysts (Table S2).[38]

To identify active sites for specific reactions, individual CO_2RR, NO_3^-RR, and HER tests were conducted. Au@Cu_2O achieves a CO faradaic efficiency (FE) of 82.14% for CO_2RR but only 12.63% FE for NH_3 generation at −0.4 V *vs.* RHE (Fig. S18). Conversely, Cu@Cu_2O delivers a high FE of 66.21% for ammonia electrosynthesis, yet a low CO FE of 5.63% at −0.4 V *vs.* RHE (Fig. S19), confirming that Cu and Au sites preferentially adsorb nitrate and CO_2, respectively. Additionally, HER activity of the core–shell catalyst is significantly lower than that of the CuAu alloy (Fig. S20), attributed to the strong *H adsorption capability of Cu sites in CuAu. We also compared the HER polarization curves of CuAu and CuAu@Cu_2O in a 1 M KCl electrolyte (pH = 3). The HER activity of CuAu@Cu_2O was significantly suppressed, highlighting the role of the Cu_2O shell in optimizing *H adsorption and promoting proton utilization for C–N coupling (Fig. S21). However, CuAu@Cu_2O retains moderate *H adsorption capacity. The HER competes with the CO_2RR and NO_3^-RR in standalone reactions, explaining the mediocre performance of the CuAu alloy compared to CuAu@Cu_2O.

Remarkably, CuAu@Cu_2O shows drastically reduced CO, NH_3, and H_2 yields but a sharp increase in urea production compared to other samples. This is ascribed to its balanced adsorption strengths for *CO, *NH_2, and *H, facilitating the coupling of *CO and *NH_2 intermediates to form *$CONH_2$, consistent with the Sabatier principle. Electrochemical impedance spectroscopy (EIS) confirms the high charge transfer efficiency of CuAu@Cu_2O (Fig. S22), attributed to its abundant active sites and optimized electronic structure, which synergistically promote balanced activation of NO_3^- and CO_2 for efficient C–N coupling.

To verify the nitrogen source in the electrochemically synthesized urea, isotope labeling experiments were performed. The electrocatalytic reaction was conducted at −0.5 V *vs.* RHE in an electrolyte containing 98% atom ^{15}N-labeled $K^{15}NO_3$ (Sigma-Aldrich). Subsequent analysis by ^1H NMR spectroscopy (Fig. 3c) revealed signals exclusively corresponding to ^{15}N-labeled urea and ^{15}N-labeled ammonia. The absence of signals from non-labeled nitrogen species and the sole presence of ^{15}N-labeled urea confirm that the nitrate ions ($^{15}NO_3^-$) in the electrolyte served as the primary nitrogen source for the urea produced in this system. Furthermore, experiments to verify the carbon source revealed that using an Ar-saturated electrolyte containing 0.2 M K_2CO_3 and 0.1 M KNO_3 yielded only

trace amounts of urea (FE < 2%), whereas continuous CO_2 bubbling in an identical electrolyte significantly enhanced urea production, achieving a rate of 1824.8 μg h^{-1} mg^{-1}. This stark contrast demonstrates that gaseous CO_2, not carbonate ions (CO_3^{2-}), serves as the essential carbon source for urea formation, confirming successful urea synthesis from nitrate (NO_3^-) and CO_2 (Fig. 3d).

The stability of the catalyst during electrochemical processes was rigorously evaluated. The morphology and crystalline structure of the CuAu@Cu_2O catalyst during electrochemical urea synthesis were investigated through TEM, XPS, and XRD characterization methods before and after electrolysis. As shown in Fig. S23, SEM and TEM images of CuAu@Cu_2O after C–N coupling at −0.5 V *vs.* RHE show negligible morphological changes, indicating no significant particle aggregation. Furthermore, XRD patterns after electrolysis confirm that CuAu@Cu_2O retains its crystalline structure (Fig. S24a), demonstrating high stability under operational conditions. Post-electrolysis XPS analysis reveals no notable changes in surface chemical states (Fig. S23b–d), while the ICP-OES results (Tables S1 and S3) before and after electrolysis confirm that the catalyst's composition remains largely unchanged, validating the structural integrity of the core–shell architecture. A 100-hour durability test at −0.5 V *vs.* RHE (Fig. S25 and Fig. 3e), with periodic electrolyte replenishment every 10 hours, confirms the commendable stability of CuAu@Cu_2O throughout the prolonged experiment.

To test the catalytic performance over a wider pH range, we conducted additional experiments at pH = 1, 2, 3, 4, and 5 (Fig. S26). The results demonstrate that the catalyst shows optimal urea faradaic efficiency (55.4%) at pH = 3. Under stronger acidic conditions (pH = 1, 2), the urea faradaic efficiency decreases to approximately 35.68% and 42.37%, primarily due to intensified hydrogen evolution reaction (HER) competition caused by excessive protons. At pH = 4 and 5, the selectivity also declines (FE ∼ 44.83% and 40.05%), likely owing to insufficient proton supply affecting the C–N coupling step. The choice of pH = 3 represents an optimal balance among multiple factors: it provides adequate protons to promote C–N coupling, avoids severe HER competition induced by excessive protonation, maintains the structural stability of the Cu_2O shell (which may partially dissolve under stronger acidic conditions), and aligns with the typical pH range of actual acidic industrial wastewater.

Investigation of the urea electrosynthesis mechanism

To gain deeper insights into the reaction mechanism of urea formation on CuAu@Cu_2O, *in situ* Raman spectroscopy was conducted to identify C–N coupling and monitor surface species during catalytic reactions. Raman spectra detected undissociated intermediates acting as substrates for the rate-determining step. As shown in Fig. S27, a distinct Raman band at 983 cm^{-1}, attributed to N–C–N vibrational modes, emerges on the CuAu@Cu_2O catalyst at −0.5 V *vs.* RHE. The ν(N–C–N) signal intensity for CuAu@Cu_2O spans the −0.3 to −0.7 V *vs.* RHE potential range, with the C–N peak's integrated area reaching a maximum at −0.5 V *vs.* RHE. Beyond this potential, the ν(N–C–N) intensity diminishes, likely due to reduced generation of the *$CONH_2$ intermediate. Adsorbed NO_3^- (1048 cm^{-1}) transforms into NO_2^- (796 cm^{-1}, $\delta(NO_2^-)$) and NH_2 (1289 cm^{-1}, $\nu(NH_2)$), confirming the NO_3^- → *NO_2^- → *NH_2 pathway.[39]

Between −0.4 and −0.6 V *vs.* RHE, vibrational signals from the *COOH intermediate (1046 cm^{-1}, CO_2 reduction) appear alongside δ(CN) (598 cm^{-1}) and ν(CN) (1388 cm^{-1}) vibrations, complemented by a ν(C═O) peak at 1719 cm^{-1}, collectively corroborating urea formation.[40] These results align with the hypothesis that *$CONH_2$ formation is the critical step in urea synthesis. Additional *in situ* Raman tests on different catalysts (Fig. 3f) reveal that *NH_2 stretching vibrations occur only in Au-containing catalysts, while ν(C═O) vibrations appear exclusively in Cu-containing catalysts. This suggests that Au and Cu sites act as active centers for adsorbing *CO and *NH_2 intermediates, respectively, consistent with the experimental findings.

DFT calculations on CuAu@Cu_2O, CuAu, Au@Cu_2O, and Cu@Cu_2O models revealed mechanistic insights into urea synthesis. The adsorption configurations of the reaction intermediates on CuAu@Cu_2O, CuAu, Cu@Cu_2O and Au@Cu_2O are shown in Fig. S28–32. For CO_2 activation, CuAu@Cu_2O exhibited a lower free energy barrier (1.418 eV) for the *COOH formation step compared to Cu@Cu_2O (1.638 eV), highlighting Au's role in facilitating CO_2 reduction (Fig. 4a). In nitrate reduction, Cu sites dominated the PCET-driven *NH_2 formation, with the *NO → *NOH step requiring 0.60 eV on CuAu@Cu_2O *versus* 0.52 eV on Au@Cu_2O, aligning with experimental observations of high NO_2^-/NH_3 selectivity. The *H adsorption energy on CuAu@Cu_2O (0.369 eV) was lower than that on CuAu (0.438 eV), demonstrating Cu_2O's capacity to supply protons for C–N coupling while suppressing the HER, as confirmed by the near-zero *H free energy on bare CuAu favoring hydrogen evolution (Fig. 4b).

Critical to urea formation, the *$CONH_2$ coupling barrier was minimized at CuAu@Cu_2O (−0.454 eV), significantly lower than Cu@Cu_2O (0.641 eV), Au@Cu_2O (−0.393 eV), and CuAu (−0.387 eV), underscoring synergistic effects among Cu (NO_3^- activation), Au (CO_2 activation), and Cu_2O (*H regulation) (Fig. 4c and d). The negative energy barrier for *$CONH_2$ formation (−0.454 eV) indicates an exothermic process that is highly spontaneous thermodynamically. This value, relative to the separated *CO and *NH_2 intermediates, reflects the stabilization energy (∼0.45 eV) generated by orbital overlap during the coupling process, which is consistent with our experimental observation of high reaction rates even at low temperatures. The further hydrogenation of *CO to form *CHO and the direct dissociation of the *NOH intermediate to form *N are both highly endergonic (with an increase in free energy). In contrast, the coupling of *CO and *NH_2 to form *$CONH_2$ exhibits a significantly negative change in free energy (ΔG = −0.454 eV), indicating that this step is spontaneous and rapid on the catalyst surface. This demonstrates that the catalyst can selectively suppress other highly competitive reduction path-

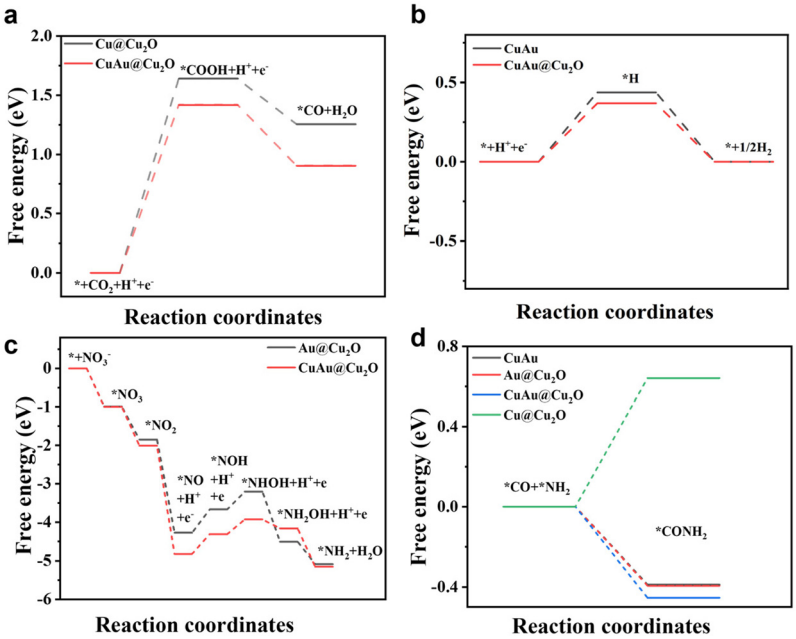

Fig. 4 Density functional theory calculations for the structural configuration and energetic reaction pathways. (a) Free energy profiles of the CO_2RR to form *CO on CuAu@Cu_2O and Cu@Cu_2O. (b) Adsorption free energies of *H on the surfaces of the CuAu@Cu_2O and CuAu catalysts. (c) Free energy profiles of the NO_3RR to form *NH_2 on CuAu@Cu_2O and Au@Cu_2O. (d) Free energy profiles of C–N coupling on CuAu@Cu_2O, CuAu, Cu@Cu_2O, and Au@Cu_2O.

ways (*e.g.*, NO_3^- → NH_4^+, CO_2 → CH_4) and direct the flow of electrons and protons toward the carbon–nitrogen coupling step to produce urea. These results collectively rationalize the catalyst's high urea selectivity and stability, with theoretical and experimental data converging on the essential roles of component synergy in intermediate optimization and HER suppression.

Conclusions

The electrocatalytic co-reduction of CO_2 and nitrate in acidic media achieves a breakthrough in urea synthesis, overcoming the limitations of carbonate formation in neutral/alkaline systems while enabling direct utilization of acidic nitrate wastewater. By engineering a porous core–shell CuAu@Cu_2O catalyst with multi-active sites, we realized 55.4% faradaic efficiency and 1824.8 μg h^{-1} mg^{-1} urea yield at −0.5 V *vs.* RHE under acidic conditions. Mechanistic insights revealed that Cu/Au dual sites synergistically reduce *COOH/*NOH adsorption energies through selective activation of CO_2 and NO_3^-, thereby driving C–N coupling. Simultaneously, the Cu_2O shell regulates proton supply *via* the optimized hydrogen adsorption strength under Au-mediated electronic modulation, aligning with the Sabatier principle to suppress the HER while promoting targeted hydrogenation. Furthermore, electron transfer from Cu to Au at the porous core–shell interface induces both charge redistribution and physical isolation effects. These effects jointly stabilize the catalyst architecture, enabling stable operation for over 100 hours against acidic corrosion and HER competition. This unique structure not only achieves high faradaic efficiency and urea yield, but also ensures 100-hour stability against acidic corrosion, establishing a new paradigm for acid-tolerant electrocatalysts and sustainable urea synthesis. Moving forward, the catalyst design strategy introduced in this study presents a promising pathway for electrocatalytic urea synthesis from nitrate in acidic industrial wastewater and CO_2. To translate this approach into practical applications, key engineering hurdles—including mass transfer limitations, product separation and purification, and long-term operational stability in reactor systems—must be overcome. Preliminary techno-economic assessment indicates that coupling wastewater treatment with the production of value-added chemicals offers economically viable opportunities, provided that efficient and scalable reactor systems are further developed.

Author contributions

L. W. and J. L.: supervised the research; J. L.: conceived the research; X. J.: designed the experiments; X. J.: performed most of the experiments and data analysis; Y. Y. and Y. G.: prepared the electrodes and helped with electrochemical measurements; Y. Y.: helped analyze physical characterization data. All authors discussed the results and commented on the manuscript.

Conflicts of interest

There are no conflicts to declare.

Data availability

All experimental data supporting this article have been included in the main text and its supplementary information (SI). Supplementary information: characterization data (SEM, TEM, XRD, XPS, *etc.*), electrochemical results, and computational details. See DOI: **https://doi.org/10.1039/d5gc04150c**.

Acknowledgements

This work was supported by the National Natural Science Foundation of China (52272222, 52072197), the Outstanding Youth Foundation of Shandong Province, China (ZR2019JQ14), the Youth Innovation and Technology Foundation of Shandong Higher Education Institutions, China (2019KJC004), the Natural Science Foundation of Shandong Province, China (ZR2021MB061), the Major Scientific and Technological Innovation Project (2019JZZY020405), the Taishan Scholar Young Talent Program (tsqn201909114), and the Major Basic Research Program of Natural Science Foundation of Shandong Province (under Grant ZR2020ZD09).

References

1 Y. Yu, Y. Sun, J. Han, Y. Guan, H. Li, L. Wang and J. Lai, *Energy Environ. Sci.*, 2024, **17**, 5183–5190.
2 Y. Wang, D. Chen, C. Chen and S. Wang, *Acc. Chem. Res.*, 2024, **57**, 247–256.
3 K. Chen, D. Ma, Y. Zhang, F. Wang, X. Yang, X. Wang, H. Zhang, X. Liu, R. Bao and K. Chu, *Adv. Mater.*, 2024, **36**, 2402160.
4 J. Liang, Q. Liu, A. A. Alshehri and X. Sun, *Nano Res. Energy*, 2022, **1**, 9120010.
5 J. Shen and D. Wang, *Nano Res. Energy*, 2024, **3**, e9120096.
6 Y. Yu, Z. Lv, Z. Liu, Y. Sun, Y. Wei, X. Ji, Y. Li, H. Li, L. Wang and J. Lai, *Angew. Chem., Int. Ed.*, 2024, **63**, e202402236.
7 Z. Lv, S. Zhou, L. Zhao, Z. Liu, J. Liu, W. Xu, L. Wang and J. Lai, *Adv. Energy Mater.*, 2023, **13**, 2300946.
8 X. Zhang, X. Zhu, S. Bo, C. Chen, M. Qiu, X. Wei, N. He, C. Xie, W. Chen, J. Zheng, P. Chen, S. P. Jiang, Y. Li, Q. Liu and S. Wang, *Nat. Commun.*, 2022, **13**, 5337.
9 X. Zhang, X. Zhu, S. Bo, C. Chen, K. Cheng, J. Zheng, S. Li, X. Tu, W. Chen, C. Xie, X. Wei, D. Wang, Y. Liu, P. Chen, S. P. Jiang, Y. Li, Q. Liu, C. Li and S. Wang, *Angew. Chem.*, 2023, **135**, e202305447.
10 X. Song, X. Ma, T. Chen, L. Xu, J. Feng, L. Wu, S. Jia, L. Zhang, X. Tan, R. Wang, C. Chen, J. Ma, Q. Zhu, X. Kang, X. Sun and B. Han, *J. Am. Chem. Soc.*, 2024, **146**, 25813–25823.
11 W. Zhong, Q. L. Hong, X. Ai, C. Zhang, F. M. Li, X. F. Li and Y. Chen, *Adv. Mater.*, 2024, **36**, 2314351.
12 A. Perazio, C. E. Creissen, J. G. R. d. l. Cruz, M. W. Schreiber and M. Fontecave, *ACS Energy Lett.*, 2023, **8**, 2979–2985.
13 W. Wu, L. Xu, Q. Lu, J. Sun, Z. Xu, C. Song, J. C. Yu and Y. Wang, *Adv. Mater.*, 2025, **37**, 2312894.
14 S. Shin, S. Sultan, Z.-X. Chen, H. Lee, H. Choi, T.-U. Wi, C. Park, T. Kim, C. Lee, J. Jeong, H. Shin, T.-H. Kim, H. Ju, H. C. Yoon, H.-K. Song, H.-W. Lee, M.-J. Cheng and Y. Kwon, *Energy Environ. Sci.*, 2023, **16**, 2003–2013.
15 Y. Gao, J. Wang, M. Sun, Y. Jing, L. Chen, Z. Liang, Y. Yang, C. Zhang, J. Yao and X. Wang, *Angew. Chem., Int. Ed.*, 2024, **63**, e202402215.
16 Y. Jiang, L. Huang, C. Chen, Y. Zheng and S.-Z. Qiao, *Energy Environ. Sci.*, 2025, **18**, 2025–2049.
17 N. Dutta and S. C. Peter, *J. Am. Chem. Soc.*, 2025, **147**, 9019–9036.
18 X. Yan, S. Yang, Y. Feng, S. Chao, P. Jia, J. Wei, L. Yang, Y. Guo and H. Zhang, *Appl. Catal., B*, 2025, **371**, 125242.
19 M. Xu, F. Wu, Y. Zhang, Y. Yao, G. Zhu, X. Li, L. Chen, G. Jia, X. Wu, Y. Huang, P. Gao and W. Ye, *Nat. Commun.*, 2023, **14**, 6994.
20 Y. Li, S. Zheng, H. Liu, Q. Xiong, H. Yi, H. Yang, Z. Mei, Q. Zhao, Z.-W. Yin, M. Huang, Y. Lin, W. Lai, S.-X. Dou, F. Pan and S. Li, *Nat. Commun.*, 2024, **15**, 176.
21 Y. Zhao, Y. Ding, W. Li, C. Liu, Y. Li, Z. Zhao, Y. Shan, F. Li, L. Sun and F. Li, *Nat. Commun.*, 2023, **14**, 4491.
22 P. Zhan, J. Zhuang, S. Yang, X. Li, X. Chen, T. Wen, L. Lu, P. Qin and B. Han, *Angew. Chem., Int. Ed.*, 2024, **63**, e202409019.
23 J. A. Kephart, B. S. Mitchell, W. Kaminsky and A. Velian, *J. Am. Chem. Soc.*, 2022, **144**, 9206–9211.
24 D. Zhou, C. Chen, Y. Zhang, M. Wang, S. Han, X. Dong, T. Yao, S. Jia, M. He, H. Wu and B. Han, *Angew. Chem., Int. Ed.*, 2024, **63**, e202400439.
25 H. Huang, H. Jung, C.-Y. Park, S. Kim, A. Lee, H. Jun, J. Choi, J. W. Han and J. Lee, *Appl. Catal., B*, 2022, **315**, 121554.
26 P. Zhang, L. Li, D. Nordlund, H. Chen, L. Fan, B. Zhang, X. Sheng, Q. Daniel and L. Sun, *Nat. Commun.*, 2018, **9**, 381.
27 F. Liu, Y. Xia, W. Xu, L. Cao, Q. Guan, Q. Gu, B. Yang and J. Lu, *Angew. Chem., Int. Ed.*, 2021, **60**, 19324–19330.
28 W. Zhan, J. Wang, H. Wang, J. Zhang, X. Liu, P. Zhang, M. Chi, Y. Guo, Y. Guo, G. Lu, S. Sun, S. Dai and H. Zhu, *J. Am. Chem. Soc.*, 2017, **139**, 8846–8854.
29 X. Feng, J. Liu, Y. Kong, Z. Zhang, Z. Zhang, S. Li, L. Tong, X. Gao and J. Zhang, *Adv. Mater.*, 2024, **36**, 2405660.
30 Y. Xiao, X. Tan, B. Du, Y. Guo, W. He, H. Cui and C. Wang, *Angew. Chem., Int. Ed.*, 2024, **63**, e202408758.
31 P. Zhan, J. Zhuang, S. Yang, X. Li, X. Chen, T. Wen, L. Lu, P. Qin and B. Han, *Angew. Chem., Int. Ed.*, 2024, e202409019, DOI: **10.1002/anie.202409019**.
32 M. Mičica, S. Ayari, M. Hemmat, M. Arfaoui, D. Vala, K. Postava, H. Vergnet, J. Tignon, J. Mangeney, S. Guo,

X. Yu, Q. J. Wang, Z. Liu, S. Jaziri, F. Carosella, R. Ferreira and S. Dhillon, *Adv. Funct. Mater.*, 2025, **35**, 2408982.
33 T. H. Jeon, S. Han, B. Kim, C. Park, W. Kim, H. Park and W. Choi, *ACS Energy Lett.*, 2021, **7**, 59–66.
34 D. A. Khurana, N. Plankensteiner, B. Vermang and P. M. Vereecken, *Angew. Chem., Int. Ed.*, 2024, **64**, e202415857.
35 P. Bessel, A. Niebur, D. Kranz, J. Lauth and D. Dorfs, *Small*, 2023, **19**, 2206379.
36 W. He, J. Chen, Q. Zhang, H. Cui and C. Wang, *Chem. Eng. J.*, 2022, **436**, 135044.
37 C. Jiao, X. Bo and M. Zhou, *J. Energy Chem.*, 2019, **34**, 161–170.
38 Z. Tan, G. Fan, L. Zheng and F. Li, *ACS Catal.*, 2024, **14**, 11218–11230.
39 X. Huang, Y. Li, S. Xie, Q. Zhao, B. Zhang, Z. Zhang, H. Sheng and J. Zhao, *Angew. Chem., Int. Ed.*, 2024, **63**, e202403980.
40 L. Lv, H. Tan, Y. Kong, B. Tang, Q. Ji, Y. Liu, C. Wang, Z. Zhuang, H. Wang, M. Ge, M. Fan, D. Wang and W. Yan, *Angew. Chem., Int. Ed.*, 2024, **63**, e202401943.